HHS Public Access

Author manuscript

Cancer Res. Author manuscript; available in PMC 2022 March 01.

Published in final edited form as:

Cancer Res. 2021 September 01; 81(17): 4417–4430. doi:10.1158/0008-5472.CAN-20-2153.

Metabolic Enzyme DLST Promotes Tumor Aggression and Reveals a Vulnerability to OXPHOS Inhibition in High-Risk Neuroblastoma

Nicole M. Anderson[1,2], **Xiaodan Qin**[3], **Jennifer M. Finan**[1], **Andrew Lam**[3], **Jacob Athoe**[3], **Rindert Missiaen**[1], **Nicolas Skuli**[1], **Annie Kennedy**[1], **Amandeep S. Saini**[3], **Ting Tao**[4,5], **Shizhen Zhu**[6], **Itzhak Nissim**[7,8], **A. Thomas Look**[9], **Guoliang Qing**[10], **M. Celeste Simon**[1,2], **Hui Feng**[3]

[1]Abramson Family Cancer Research Institute, University of Pennsylvania Perelman School of Medicine, Philadelphia, Pennsylvania

[2]Department of Cell and Developmental Biology, University of Pennsylvania, Philadelphia, Pennsylvania

[3]Departments of Pharmacology and Medicine, Section of Hematology and Medical Oncology, The Center for Cancer Research, Boston University School of Medicine, Boston, Massachusetts

[4]National Clinical Research Center for Child Health, National Children's Regional Medical Center, Children's Hospital, Zhejiang University School of Medicine, Hangzhou, Zhejiang, China

[5]Cancer Center, Zhejiang University, Hangzhou, Zhejiang, China

[6]Department of Biochemistry and Molecular Biology, Mayo Clinic College of Medicine, Mayo Clinic Cancer Center, Rochester, Minnesota

[7]Division of Genetics and Metabolism, Children's Hospital of Philadelphia, Philadelphia, Pennsylvania

[8]Department of Pediatrics, Biochemistry, and Biophysics, University of Pennsylvania, Philadelphia, Pennsylvania

Corresponding Authors: Hui Feng, Departments of Pharmacology and Medicine, Boston University School of Medicine, The Cancer Center, 72 East Concord St. K-712A, Boston, MA, 02118. huifeng@bu.edu; and M. Celeste Simon, Abramson Family Cancer Research Institute, University of Pennsylvania, 456 BRBII/III, 421 Curie Blvd., Philadelphia, PA 19104. celeste2@pennmedicine.upenn.edu.

Authors' Contributions

N.M. Anderson: Conceptualization, formal analysis, funding acquisition, validation, investigation, visualization, methodology, writing–original draft, writing–review and editing. **X. Qin:** Formal analysis, investigation, methodology, writing–review and editing. **J.M. Finan:** Investigation, writing–review and editing. **A. Lam:** Formal analysis, investigation, writing–review and editing. **J. Athoe:** Formal analysis, investigation, writing–review and editing. **R. Missiaen:** Investigation, writing–review and editing. **N. Skuli:** Investigation, writing–review and editing. **A. Kennedy:** Investigation, writing–review and editing. **A.S. Saini:** Investigation. **T. Tao:** Resources, methodology, writing–review and editing. **S. Zhu:** Resources, methodology, writing–review and editing. **I. Nissim:** Resources, formal analysis, validation, investigation, methodology. **A. Look:** Resources, methodology, writing–review and editing. **G. Qing:** Resources, formal analysis, investigation, methodology, writing–review and editing. **M. Simon:** Conceptualization, resources, supervision, funding acquisition, validation, writing–original draft, project administration, writing–review and editing. **H. Feng:** Conceptualization, resources, supervision, funding acquisition, validation, methodology, writing–original draft, project administration, writing–review and editing.

Note: Supplementary data for this article are available at Cancer Research Online (http://cancerres.aacrjournals.org/).

[9]Department of Pediatric Oncology, Dana-Farber Cancer Institute, Boston, Massachusetts

[10]Frontier Science Center for Immunology & Metabolism, Medical Research Institute, Wuhan University, Wuhan, Hubei, China

Abstract

High-risk neuroblastoma remains therapeutically challenging to treat, and the mechanisms promoting disease aggression are poorly understood. Here, we show that elevated expression of dihydrolipoamide S-succinyltransferase (DLST) predicts poor treatment outcome and aggressive disease in patients with neuroblastoma. DLST is an E2 component of the α-ketoglutarate (αKG) dehydrogenase complex, which governs the entry of glutamine into the tricarboxylic acid cycle (TCA) for oxidative decarboxylation. During this irreversible step, αKG is converted into succinyl-CoA, producing NADH for oxidative phosphorylation (OXPHOS). Utilizing a zebrafish model of MYCN-driven neuroblastoma, we demonstrate that even modest increases in DLST expression promote tumor aggression, while monoallelic *dlst* loss impedes disease initiation and progression. DLST depletion in human MYCN-amplified neuroblastoma cells minimally affected glutamine anaplerosis and did not alter TCA cycle metabolites other than αKG. However, DLST loss significantly suppressed NADH production and impaired OXPHOS, leading to growth arrest and apoptosis of neuroblastoma cells. In addition, multiple inhibitors targeting the electron transport chain, including the potent IACS-010759 that is currently in clinical testing for other cancers, efficiently reduced neuroblastoma proliferation *in vitro*. IACS-010759 also suppressed tumor growth in zebrafish and mouse xenograft models of high-risk neuroblastoma. Together, these results demonstrate that DLST promotes neuroblastoma aggression and unveils OXPHOS as an essential contributor to high-risk neuroblastoma.

Introduction

Neuroblastoma is the most common extracranial solid tumor in children, which accounts for 7.5% of all pediatric cancer and 10% of childhood cancer deaths (1–4). As a neuroendocrine tumor, neuroblastoma arises from developing neural crest cells, which give rise to the peripheral sympathetic nervous system. Primary tumors are commonly located within the adrenal medulla, but can arise anywhere along with the sympathetic ganglia from the neck to pelvis (2, 4). Neuroblastoma is highly aggressive and approximately 50% of patients exhibit metastatic disease at diagnosis (2, 3). Despite intense multimodal therapy, only 40% of patients with high-risk neuroblastoma achieve long-term durable responses (4). Therefore, improving our understanding of the mechanisms underlying neuroblastoma aggression is critical to identify targetable pathways for therapeutic intervention.

The MYC family of oncogenes plays a pivotal role in neuroblastoma pathogenesis. *MYCN*-amplification, an established genetic marker for high-risk disease, occurs in 20% of neuroblastoma and predicts increased tumor progression and poor patient survival (1, 5). *c-MYC* is also upregulated in a distinct subset of patients with high-risk neuroblastoma (11%) resulting from focal amplifications of distal enhancers or chromosomal rearrangements that juxtapose highly active enhancers next to the *MYC* locus (6). In addition, anaplastic lymphoma kinase is the most frequently mutated gene in high-risk neuroblastoma and has

been shown to synergize with *MYCN* to increase disease aggression in animal models (7–9). In zebrafish, *MYCN* overexpression driven by the dopamine β-hydroxylase (*dβh*) promoter is sufficient to induce neuroblastoma that recapitulates the human disease genetically and histologically (6, 7, 10). *LMO1* (LIM-domain-only) was identified in a genome-wide association study as a neuroblastoma susceptibility gene that promotes metastasis in the zebrafish model of MYCN-driven neuroblastoma (11, 12).

Dysregulated MYC family members transcriptionally regulate a broad range of cellular processes to promote tumorigenesis in numerous human cancers (13–16). Cancer cells often alter their metabolism to meet the heightened nutrient requirements imposed by uncontrolled proliferation and adverse tumor microenvironments (13). In high-risk neuroblastoma, MYCN rewires metabolic programs, including elevated dependence on glutamine to replenish tricarboxylic acid (TCA) cycle intermediates (14–16). The α-ketoglutarate (αKG) dehydrogenase complex (KGDHC) catalyzes an irreversible step in the TCA cycle, converting αKG into succinyl-CoA while producing NADH for oxidative phosphorylation (OXPHOS; ref. 17). Interestingly, previous studies highlighted components of KGDHC as critical contributors to cancer evolution. For example, unbiased genetic screens identified loss of dihydrolipoamide S-succinyltransferase (DLST), oxoglutarate dehydrogenase (OGDH), and dihydrolipoamide dehydrogenase (DLD) as vulnerabilities in cancer cells, including those with PI3K mutations (18, 19). Interestingly, KGDHC has also been detected in the nucleus of glioblastoma cells, producing succinyl-CoA to modify histones (20). Loss-of-function mutations within the *DLST* catalytic domain responsible for oncometabolite generation were recently isolated in pheochromocytoma and paraganglioma (21). Finally, DLST has been shown to mediate MYC-driven leukemogenesis (22). However, its role in neuroblastoma pathogenesis has not been previously investigated.

Here, we demonstrate that elevated *DLST* expression predicts poor survival and disease aggression among neuroblastoma patients, while correlating with an increased OXPHOS gene signature. Employing a zebrafish model of MYCN-driven neuroblastoma, we show that elevated *DLST* expression promotes neuroblastoma growth and metastatic spread. Moreover, both human and zebrafish neuroblastoma cells depend on DLST for growth and survival, and its loss results in apoptotic cell death. DLST depletion in human neuroblastoma cells suppresses OXPHOS as a result of reduced cellular NADH production, and targeting OXPHOS through electron transport chain (ETC) inhibitors decreases tumor cell viability. Importantly, IACS-010759, a potent small-molecule inhibitor of the ETC complex I currently in clinical trials for treating other cancers (NCT #02882321 and #03291938), suppresses the growth of human neuroblastoma cells *in vitro* and *in vivo*. Collectively, our study demonstrates that DLST promotes neuroblastoma aggression and unveils OXPHOS as a novel therapeutic target for high-risk neuroblastoma.

Materials and Methods

Immunohistochemistry staining

Primary human neuroblastoma tumors were obtained from the Pathology Core of Tongji Hospital with informed consent and approval [number: [2014]IEC(S013)] from the Clinical

Research Ethics Committee of Tongji Medical School. We obtained "informed written consent" from the subjects (wherever necessary).

Zebrafish tumor surveillance and xenograft assays

Zebrafish (Danio rerio) husbandry was performed as described previously (23), in the aquatic facility at Boston University School of Medicine in accordance with Institutional Animal Care and Use Committee-approved protocols. More details can be found in the Supplementary Information.

Cell culture and lentiviral transduction

All cell lines except KELLY (from Sigma) were purchased from ATCC. Cell lines are routinely tested to confirm *Mycoplasma* negative status. KELLY, SK-N-BE(2), IMR-32, SK-N-AS, SK-N-FI, and BE (2)-C were maintained in RPMI1640 (Thermo Fisher Scientific: #11875–085) with other cell lines growing in DMEM (Thermo Fisher Scientific: #11965–084). Both media were supplemented with 10% FBS (GEMINI: #900–108) and 2 mmol/L of L-glutamine (Thermo Fisher Scientific: #25030–081). All cells were cultured in 37°C, 5% CO_2 humidified incubators.

Lentivirus was produced by transfecting 2.5×10^6 293T cells with 10 μg hairpin-expressing plasmid (pKLO.1), 2.5 μg pRSV-REV, 6.5 μg pMDL, and 3.5 μg pCMV-VSV-G plasmids using FUGENE 6 Transfection Kit (Promega: #E2691). The virus was harvested 24 and 48 hours after transfection. Infection was performed by incubating cells with media containing virus and 8 μg/mL polybrene (Sigma: #107689) for 12 hours. Cells were recovered in complete medium for 24 hours and selected with puromycin for 36 hours. The control (*shScramble*) and *shDLST24* hairpins were purchased from Addgene (#1864) and Dharmacon (#TRCN0000035424), respectively, with *shDLST1* hairpin (5′-CCCTAGTGCTGGTATACTATA-3′) generated previously (22).

Seahorse assay

The mitochondrial respiratory capacity was determined with the XF Cell Mito Stress Test Kit (Agilent Technologies: #103015–100). KELLY cells were seeded in the XF96 cell culture microplate at a density of 3×10^4 per well with replicates of 6 to 12 for the following groups: DLST depletion: *shScramble, shDLST1,* and *shDLST24*; IACS treatment: vehicle, 10 nmol/L, and 100 nmol/L. XF96 FluxPak sensor cartridge was hydrated with Seahorse Calibrant overnight in a non-CO_2 incubator at 37°C. The following day, cells were incubated with the Seahorse medium (plus 2 mmol/L L-glutamine, 1 mmol/L sodium pyruvate, and 10 mmol/L glucose) for 1 hour prior. The OCR was measured by XFe96 extracellular flux analyzer with the sequential injection of 1 μmol/L oligomycin A, 0.25 μmol/L FCCP, and 0.5 μmol/L rotenone/antimycin A. After the experiment, the OCR value in each well was normalized to the protein concentration determined by a Pierce BCA Protein Assay Kit (Thermo Fisher Scientific: #23225).

Murine xenograft

Xenograft experiments were approved by the Animal Care and Use Committee at the University of Pennsylvania. KELLY cells (3×10^6) were injected in a 1:1 mixture of

PBS and Matrigel (Corning; #356234) in a final volume of 200 μL into both flanks of female Balb/c nude mice (Charles River Laboratories: #194). Flank tumors were measured every other day by electronic calipers and tumor volumes were calculated as (π/6)(length × width^2). Once the tumor reached approximately 100 mm^3, mice were randomly assigned to two groups and treated with vehicle or IACS-010759 (Selleck-chem: #S8731). The vehicle (containing 0.5% Methyl Cellulose; viscosity: 4000cP; Sigma: no. M0512) or IACS-010759 (7.5 mg/kg per dose) was given to mice by oral gavage once daily on a 5-day on 2-day off regimen as described (24). At the endpoint of the experiments, animals were euthanized by CO_2 inhalation.

Statistical analysis

All statistical analyses were performed with GraphPad Prism 8.0 using unpaired two-tailed *t* tests unless otherwise stated. All data are represented as mean ± SEM. Statistical analysis of zebrafish tumor onset curves was performed by the log-rank Mantel–Cox test. Kaplan–Meier curves of human expression data were analyzed in the R2: genomics analysis and visualization platform. The "Hallmark signatures" gene set was used for gene set enrichment analysis (GSEA). Normalized enrichment scores (NES) were determined. Statistical significance was defined as *, $P < 0.05$; **, $P < 0.01$; ***, $P < 0.001$; ****, $P < 0.0001$, *, FDR < 0.05.

Results

High *DLST* expression is associated with poor treatment outcomes and aggressive disease in patients with neuroblastoma

To assess the involvement of DLST in human neuroblastoma, we analyzed publicly available datasets for the association of *DLST* expression with patient outcomes. We found that high *DLST* expression in patients with neuroblastoma predicts poor event-free and overall survival (SEQC, an RNA-SEQ dataset containing 498 patient samples; Fig. 1A and B; ref. 25). Our reanalysis of two additional datasets validated DLST's prediction on event-free survival (Versteeg and Kocak, containing 88 and 476 patient samples, respectively; Supplementary Fig. S1A–S1D) and overall survival (Versteeg; Supplementary Fig. S1B; ref. 26). Given that *MYCN*-amplification only represents a fraction of high-risk patients, we next determined whether high *DLST* expression predicts prognosis in nonamplified patients. Analysis of a patient cohort without *MYCN*-amplification revealed that high *DLST* expression is associated with both increased risk of disease relapse and patient death (Fig. 1C and D; Supplementary Fig. S1E and S1F). However, high *DLST* expression could not further segregate overall or event-free survival among patients with aggressive *MYCN*-amplified neuroblastoma (Supplementary Fig. S1G and S1H). To further our analysis, we immunostained patient samples and found that DLST protein levels are significantly increased in most tumor cells of stage IV primary neuroblastoma samples, compared with stage I/II tumor samples (Fig. 1E). Collectively, we demonstrated that high *DLST* expression is associated with poor treatment outcomes and increased tumor aggression among neuroblastoma patients.

DLST overexpression promotes MYCN-driven neuroblastoma aggression in zebrafish

Given high *DLST* expression predicted both poor treatment outcomes and tumor aggression among patients with neuroblastoma, we next asked whether *DLST* overexpression can cooperate with enhanced MYCN activity in neural crest cells (one category of high-risk disease) to promote tumor progression. A zebrafish model of MYCN-driven neuroblastoma (MYCN_TT), in which human *MYCN* is expressed under the control of the zebrafish *dβh* promoter, was utilized to address this question (27). The MYCN_TT zebrafish line is highly aggressive, with neuroblastoma initiation as early as 5-week postfertilization (wpf) and >80% tumor penetrance at 30 weeks of age (27). Human *DLST* was introduced into zebrafish neural crest cells through microinjection of a *Tg*(*dβh:DLST*) construct into one-cell-stage *MYCN* embryos, with sibling embryos microinjected with a *Tg*(*dβh:mCherry*) construct as controls.

Beginning at 5-wpf, DLST_OE;MYCN_TT (*dβh*:DLST;MYCN_TT) fish and their MYCN_TT siblings (*dβh*:mCherry;MYCN_TT) were screened weekly by fluorescent microscopy for tumor development as previously described (27). Despite robust tumor development in the MYCN_TT zebrafish line, *DLST* overexpression was sufficient to promote earlier tumor onset (Fig. 2A). However, in the absence of *MYCN* overexpression, *DLST* overexpression alone was insufficient to induce tumor formation (Fig. 2A). By 17-wpf, tumors developed in 97% of DLST_OE;MYCN_TT fish compared with 87% of MYCN_TT fish. When disease burden was quantified based on fluorescence intensity at 6-wpf, we found that *DLST* overexpression led to a significant increase in tumor burden in DLST_OE;MYCN_TT fish (Fig. 2B), together with the presence of tumor cells in the distal abdominal locations that were absent in MYCN_TT fish.

Next, we stained serially sectioned 6-wpf DLST_OE;MYCN_TT and MYCN_TT fish for hematoxylin and eosin and tyrosine hydroxylase (TH) staining in adjacent sections to detect ectopic neuroblastoma cells. Besides the primary site, tumor cells were also detected in distant locations, including mid-kidney, hind-kidney, spleen, eyes, and gills (Fig. 2C and D; Supplementary Fig. S2A and S2B). The frequency of sites with disseminated tumor cells was five-fold higher in DLST_OE;MYCN_TT fish compared with those in MYCN_TT fish (Fig. 2E; Supplementary Fig. S2C; Supplementary Table S1). Metastases in the eyes and gills were only identified in DLST_OE;MYCN_TT fish at 6-wpf and the incidence of metastasis in the spleen and hind kidney was also significantly higher in *DLST*-overexpressing fish (Supplementary Fig. S2C; Supplementary Table S1). DLST expression is significantly upregulated in MYCN_TT tumor cells compared with cells of origin in the IRG (Supplementary Fig. S2D). Remarkably, DLST_OE;MYCN_TT tumors had only 2-fold increased DLST expression compared with MYCN_TT tumors (Fig. 2F). Together, our data demonstrate that even modest changes in DLST abundance collaborate with MYCN to promote neuroblastoma aggression, as demonstrated by faster onset, increased tumor burden, and higher frequency of disseminated disease.

Heterozygous loss of *dlst* delays MYCN-driven neuroblastoma onset and decreases disease aggression in zebrafish

Having established that *DLST* overexpression can promote disease aggression in MYCN-driven neuroblastoma, we next asked how DLST depletion may impact MYCN-driven neuroblastoma development in zebrafish. To address this question, we bred the MYCN_TT fish to loss-of-function *dlst* mutant zebrafish, in which the *dlst* locus was disrupted by a retroviral insertion (28). Because heterozygous loss of *dlst* does not alter normal zebrafish development, fertility, or gross morphology (22), we examined MYCN-driven neuroblastoma development in heterozygous fish. Beginning at 5-wpf, offspring were assessed weekly by fluorescent microscopy for evidence of tumor development. Of note, monoallelic loss of *dlst* was sufficient to delay MYCN-driven neuroblastoma onset and decrease disease penetrance: 62% MYCN_TT; *dlst*+/− fish had tumors compared with 83% in the control MYCN_TT fish at 30-wpf (Fig. 3A). Western blotting analysis confirmed that *dlst* heterozygous loss led to approximately a 50% reduction of Dlst protein levels, as expected (Fig. 3B; Supplementary Fig. S2D). Given that *DLST* overexpression promoted tumor aggression in our MYCN-driven zebrafish model of neuroblastoma, we next determined whether *dlst* heterozygous loss could suppress tumor aggression. Although *dlst* heterozygous loss did not change tumor burden (Fig. 3C), MYCN_TT; *dlst*+/− fish had a significant reduction in the number of metastatic sites at 10-wpf (Fig. 3D; Supplementary Fig. S3H).

To investigate cellular mechanisms responsible for the effects of *dlst* allelic loss on neuroblastoma development, we evaluated three main impacting factors: proliferation, differentiation, and apoptosis, for *MYCN*-overexpressing neural crest cells (premalignant cells) within the interrenal gland (IRG) at 3-wpf in MYCN_TT and MYCN_TT; *dlst*+/− fish. First, we assessed premalignant cells for alterations in proliferation or differentiation and found no changes for phosphohistone 3 (pH3) or TH staining in *dlst*± fish (Supplementary Fig. S3A–S3F). However, heterozygous loss of *dlst* increased apoptosis of premalignant cells at 3-wpf as assessed by activated caspase-3 immunostaining (Fig. 3E and F; Supplementary Fig. S3G). Therefore, allelic loss of *dlst* delays tumor onset by inducing apoptosis in *MYCN*-overexpressing premalignant neural crest cells at 3-wpf and reduces tumor aggression.

DLST depletion by RNAi slows the growth and induces apoptosis of human neuroblastoma cells

To determine whether DLST loss represents a vulnerability in human neuroblastoma cells, we inactivated *DLST* using two independent hairpins in eight human neuroblastoma cell lines with or without *MYCN*-amplification (Fig. 4A and B; Supplementary Fig. S4A and S4B). DLST depletion slowed cell growth in all *MYCN*-amplified cell lines (KELLY, SK-N-BE[2], BE[2]-C, and SK-N-DZ) and two non–*MYCN*-amplified cell lines (SHEP and SK-N-FI; Fig. 4A and B). Interestingly, although SK-N-SH and SK-N-AS had a similar growth rate as other non–*MYCN*-amplified cell lines, they were largely insensitive to DLST loss (Fig. 4A and B; Supplementary Fig. S4C). To elucidate the cellular mechanisms underlying decreased cell growth, we performed Annexin-V and PI staining in KELLY, SK-N-BE(2), SK-N-FI, and SK-N-SH cells. DLST depletion induced apoptosis in KELLY, SK-N-BE(2),

and SK-N-FI cells but not in insensitive SK-N-SH cells (Fig. 4C; Supplementary Fig. S4D). In addition, alterations in cell cycle occurred in most of these cell lines, with very modest changes observed in SK-N-SH cells (Fig. 4D; Supplementary Fig. S4E). Despite no effect on the growth of the non–*MYCN*-amplified cell line SK-N-AS, DLST depletion impeded their migration in a scratch wound assay (Supplementary Fig. S4F). Collectively, these data demonstrate that a majority of neuroblastoma cell lines are sensitive to DLST depletion, undergoing a G_1 cell-cycle arrest and apoptosis, regardless of their *MYCN* amplification status.

DLST inactivation reduces NADH and suppresses OXPHOS

MYCN-amplified neuroblastoma cells are addicted to glutamine and utilize glutamine-derived metabolites to replenish the TCA cycle (i.e., glutamine anaplerosis; ref. 15). Given that DLST/KGDHC is an entry point for glutamine-derived metabolites into the TCA cycle, we utilized a stable-isotope labeled glutamine tracer (U-^{13} C-glutamine) to assess the effect of *DLST* inactivation on glutamine anaplerosis at day 3.5 postinfection (Fig. 5A). This timepoint was chosen to avoid any confounding influences of cell cycle arrest and death observed at later times after DLST depletion. Upon DLST loss (especially via the more effective *shDLST1* hairpin), glutamine-derived carbons in succinate, fumarate, and malate were significantly reduced in *MYCN*-amplified SK-N-BE(2) and KELLY cells (Fig. 5A and B; Supplementary Fig. S5A and S5B), indicating that oxidative decarboxylation of glutamine carbons is restricted. When total intracellular levels of TCA cycle intermediates were quantified, we found that DLST depletion resulted in a moderate increase in intracellular αKG without affecting other cycle intermediates (Fig. 5C; Supplementary Fig. S5C and S5D). Intriguingly, we found that DLST knockdown resulted in an increase in L-2-hydroxyglutarate (L-2-HG) in SK-N-BE(2) and KELLY, suggesting that excess αKG is being diverted into other metabolic pathways, including the formation of L-2-HG (Fig. 5C; Supplementary Fig. S5D).

To understand whether restoration of the TCA cycle downstream of KGDHC rescued cell growth upon DLST depletion, we supplemented culture media with methyl-succinate, a cell-permeable form of succinate (29). Surprisingly, the addition of methyl-succinate at multiple concentrations failed to rescue growth defects in *MYCN*-amplified KELLY cells upon DLST depletion (Supplementary Fig. S5E). If anything, methyl-succinate supplementation reduced KELLY cell growth, although the changes failed to reach statistical significance. The implications of these findings will be further elaborated on in the Discussion. Besides the TCA cycle intermediate succinyl-CoA, the irreversible reaction catalyzed by DLST/KGDHC also generates NADH (Fig. 5A). Hence, we assessed the effect of DLST loss on intracellular pools of NAD^+ and NADH. Upon *DLST* inactivation, intracellular NADH was significantly reduced, resulting in increased NAD+/NADH ratios in SK-N-BE(2), KELLY, and SK-N-FI cells but not in resistant SK-N-SH cells (Fig. 5D and E; Supplementary Fig. S5F and S5G). Because NADH feeds into the ETC for ATP production (17), we determined the effects of DLST inhibition on OXPHOS. DLST inhibition suppressed OXPHOS in SK-N-BE(2), KELLY, SK-N-FI, and SK-N-SH cells, as demonstrated by significantly reduced oxygen consumption rates (OCR) at basal, ATP-linked, and maximal respiration levels (Fig. 5F and G; Supplementary Fig. S5H and S5I). Interestingly, DLST depletion also

significantly suppressed glycolysis in SK-N-BE(2), KELLY, and SK-N-FI cells as assessed by basal extracellular acidification rate (ECAR; Fig. 5H).

To determine whether DLST promotes neuroblastoma aggression through OXPHOS, we analyzed publicly available transcriptional data from high-risk patients (both *MYCN*-amplified and non-amplified; SEQ-C; ref. 25), comparing the transcriptomes of DLST-high (4th-quartile) versus DLST-low (1st-quartile) samples. GSEA revealed an increase in gene signatures for E2F targets, MYC targets, OXPHOS, and DNA repair pathways (Supplementary Fig. S5J). Importantly, high DLST expression within patients with high-risk neuroblastoma correlates with significant enrichment of genes within an OXPHOS signature (Supplementary Fig. S5K). Together, our data demonstrate that DLST depletion in neuroblastoma cells minimally impacts glutamine anaplerosis yet significantly reduces NADH and suppresses OXPHOS, suggesting that OXPHOS may mediate neuroblastoma tumor aggression.

Human neuroblastoma cells are sensitive to inhibition of complex I in the ETC

To further elucidate the involvement of OXPHOS in neuroblastoma pathogenesis, we queried the SEQC dataset to compare the expression of OXPHOS genes in high-risk versus low-risk neuroblastoma patient samples by GSEA (25). OXPHOS gene expression is significantly enriched in high-risk neuroblastoma samples (Supplementary Fig. S6A). To learn whether OXPHOS suppression is consistent with decreased cell growth upon DLST depletion, we treated a panel of human neuroblastoma cell lines with rotenone (a classic ETC complex I inhibitor). Most of these cell lines were highly sensitive to rotenone treatment with IC_{50}s of less than 1 μmol/L, except SK-N-FI (IC_{50}: 1.25 μmol/L; Supplementary Fig. S6B). When neuroblastoma cell lines KELLY, SK-N-BE(2), and SK-N-FI were tested for sensitivity to inhibitors of other ETC components, such as complex III (antimycin) and ATP-synthase (oligomycin A), *MYCN*-amplified KELLY and SK-N-BE(2) were highly sensitive to the treatment, whereas *MYCN*-nonamplified SK-N-FI was relatively resistant (Supplementary Fig. S6C).

To determine whether OXPHOS inhibition could in principle serve as a therapeutic strategy for neuroblastoma, we employed a potent and specific inhibitor of complex I, IACS-010759 (IACS), currently in phase I clinical trials for treating acute myeloid leukemia (AML) and adult solid tumors (NCT #02882321 and #03291938). Five days of IACS treatment in most neuroblastoma cell lines resulted in a dose-dependent decrease in cell growth with IC-50s in the nanomolar range, except for SK-N-FI and SK-N-AS (Fig. 6A). In KELLY, SK-N-BE(2), SK-N-DZ, and SK-N-FI cells, 24-hour treatment with 10 or 100 n mol/L of IACS significantly suppressed OCR; whereas up to 100 nmol/L was needed to suppress OCR in SK-N-SH (Fig. 6B; Supplementary Fig. S6D and S6E). Interestingly, IACS treatment led to an increase in basal ECAR, indicating the compensatory effects of these cells to enhance glycolysis for ATP production (Supplementary Fig. S6F). IACS treatment induced apoptosis of KELLY, SK-N-BE(2), SK-N-DZ, SK-N-SH, and SK-N-FI cells in a dose-dependent manner (Fig. 6C; Supplementary Fig. S6G). Our data demonstrate that human neuroblastoma cells are highly sensitive to the suppression of OXPHOS.

Besides reducing NADH to suppress OXPHOS, DLST depletion surprisingly alters intracellular αKG metabolism and leads to the production of L-2-HG (Fig. 5C). The cell permeable form of αKG, dimethyl α-ketoglutarate (DMKG), is readily taken up by cells and can be converted into 2-HG (Fig. 5C; Supplementary Fig. S5D; ref. 30). It was previously shown that ETC inhibition synergizes with DMKG and results in the death of cancer cells both *in vitro* and *in vivo* (30). To understand whether OXPHOS suppression alone or in combination with changes in αKG levels impedes neuroblastoma cell growth, we next treated four neuroblastoma cell lines with IACS, DMKG, or the combination of both. After 48-hour treatment, we found that DMKG alone was sufficient to impair the growth of *MYCN*-amplified cell lines (KELLY, SK-N-BE(2), SK-N-DZ). The combination of IACS and DMKG resulted in a striking synergy in SK-N-BE(2), KELLY, SK-N-DZ, SK-N-FI, SHEP, and BE(2)-C (Fig. 6D; Supplementary Fig. S6H). In contrast, the SK-N-SH and SK-N-AS cell line were insensitive to all treatments (Fig. 6D; Supplementary Fig. S6H). These findings recapitulate the sensitivity of neuroblastoma cell lines to DLST depletion. Interestingly, overexpressing *MYCN* in the non–*MYCN*-amplified cell line, SK-N-AS, was not sufficient to sensitize to the combination treatment of DMKG and IACS (Supplementary Fig. S6I). The unexpected results of αKG treatment will be discussed later. Together, our data show that OXPHOS is critical for neuroblastoma cell growth and survival, while excess αKG is toxic to *MYCN*-amplified neuroblastoma cells.

OXPHOS inhibition by IACS reduces aggression of *MYCN*-amplified neuroblastoma in xenografts

Our *in vitro* findings indicated that human neuroblastoma cells are highly sensitive to OXPHOS inhibition through ETC inhibitor treatment, the novel complex I inhibitor IACS in particular. Subsequently, we utilized the zebrafish xenograft model to study IACS's effect on neuroblastoma cells *in vivo*. We first tested the ability of IACS to inhibit the growth of MYCN_TT cells. Four days of IACS treatment was sufficient to suppress the growth of MYCN-TT neuroblastoma cells in zebrafish xenografts (Fig. 7A and B). We then assessed the ability of IACS to suppress the growth of human neuroblastoma cells in zebrafish xenografts. IACS treatment slowed the growth of KELLY, SK-N-BE(2), and SK-N-DZ cells yet had no effect on SK-N-SH cells, which recapitulated our *in vitro* results (Fig. 7A and B; Supplementary Fig. S7A). The cellular mechanism underlying slowed growth in KELLY zebrafish xenografts was decreased proliferation as demonstrated by a reduction in Ki67-positive cells upon IACS treatment (Supplementary Fig. S7B).

We also applied a murine xenograft model to assess the ability of IACS to inhibit the growth of KELLY cells *in vivo*. After KELLY tumors grew to approximately 100 mm^3, mice were treated with either vehicle or 7.5 mg/kg IACS. IACS treatment significantly slowed the growth of tumors and resulted in decreased tumor size and weight (Fig. 7C). Importantly, IACS treatment did not alter the body weight of treated mice, suggesting that it was well tolerated in these animals over this period. Histologic analysis revealed that IACS treatment decreased tumor cell proliferation, as demonstrated by fewer pH3 positive cells (Fig. 7D). Specifically, IACS treatment slowed the growth of tumor cells by inducing a G_1 cell-cycle arrest, as evident by increased p21 positive cells (Fig. 7E). In contrast to the effects of IACS on *in vitro* growth, cleaved caspase-3 (CC3) staining revealed no evidence

of apoptosis upon IACS treatment in xenograft tumors (Supplementary Fig. S7C), likely due to a relatively short time frame of treatment. These data demonstrate that OXPHOS represents a vulnerability for neuroblastoma and IACS administration can reduce tumor aggression by slowing tumor cell proliferation.

Discussion

High-risk neuroblastoma is an extremely aggressive disease. Patients with neuroblastoma that present with metastases fall within the high-risk category and represent a significant challenge to treat. Only a limited number of factors have convincingly been shown to promote the full range of tumor progression (11, 12). Improved understanding of neuroblastoma pathogenesis and the identification of novel contributors to disease aggression could facilitate the development of therapeutic strategies to treat these patients. Here, we show that elevated *DLST* expression not only predicts poor patient outcomes, but also disease aggression in human neuroblastoma. Utilizing a zebrafish model of MYCN-driven neuroblastoma, we found that even a modest increase in DLST protein levels can synergize with MYCN to accelerate neuroblastoma onset, increase tumor burden, and promote metastasis. Conversely, a 50% reduction of DLST induces apoptosis of *MYCN*-overexpressing neural crest cells, impairs neuroblastoma initiation, and suppresses tumor aggression. DLST depletion in human neuroblastoma cells decreases cell growth and induces apoptosis. Together, our studies pinpoint DLST as a novel contributor to disease aggression in high-risk neuroblastoma.

DLST loss together with other KGDHC components has been identified as a vulnerability in MYC-driven leukemia and PIK3CA mutant cancer cells (18, 22). Utilizing two independent models of neuroblastoma (transgenic zebrafish and human cell lines), we demonstrated that DLST inhibition represents a vulnerability in neuroblastoma. DLST/KGDHC catalyzes an irreversible reaction in the TCA cycle, serving as a critical entry point for glutamine anaplerosis (17). *MYCN*-amplified neuroblastoma cells utilize glutamine metabolites to fuel the TCA cycle and depend on glutamine for survival (15, 31). Interestingly, glutamine anaplerosis was minimally disrupted in *MYCN*-amplified neuroblastoma cells upon DLST depletion and the addition of the downstream TCA cycle intermediate succinate failed to rescue growth defects. This phenotype is different from MYC-driven T-cell leukemia, in which the addition of methyl-succinate leads to a robust rescue of cell growth (22). The fact that methyl-succinate fails to rescue neuroblastoma cell growth is likely due to the notable dependence of these cells on NADH. Indeed, DLST depletion in neuroblastoma cells drastically reduces NADH, leading to an increase of NAD/NADH ratio and OXPHOS suppression. In contrast, OGDH depletion in the context of PI3K mutations results in a reduction of NAD/NADH ratio. Mutations in PI3K also do not sensitize cancer cells to OXPHOS inhibition (30). Collectively, these data suggest that KGDHC components can exert different functions, likely impacted by oncogenic drivers and/or tissues of origin.

KGDHC catalyzes an irreversible reaction within the TCA cycle converting αKG into succinyl-CoA while producing NADH (17). We show that DLST loss inhibits the ETC through the reduction of NADH levels and increases total intracellular αKG in human neuroblastoma cells, while minimally impacting other cycle intermediates. Moreover,

supplementation of DMKG (a cell-permeable ester of αKG) is cytotoxic to *MYCN*-amplified, but not nonamplified neuroblastoma cells. Importantly, DMKG synergizes with OXPHOS inhibition to kill neuroblastoma cells that are sensitive to DLST depletion regardless of their *MYCN*-amplification status. DLST loss-of-function mutations lead to dysregulated αKG metabolism and result in the production of L-2-HG (32). We found that DLST depletion in SK-N-BE(2) and KELLY cells also led to a significant increase in L-2-HG levels, providing an explanation for where excessive αKG is shuttled. We believe that excess αKG together with OXPHOS inhibition phenocopies the effects of DLST depletion in neuroblastoma cells, as DMKG and IACS treatment recapitulates the sensitivity of neuroblastoma cells to DLST knockdown. DLST depletion also suppresses glycolysis in neuroblastoma cells as evidenced by reduced basal ECAR (Supplementary Fig. S7D). Both αKG and L-2-HG can regulate the αKG–dependent dioxygenases, a class of enzymes known to modify gene transcription and reprogram cellular metabolism (33). Therefore, the build-up of αKG and L-2-HG in neuroblastoma cells upon DLST depletion may impact some of these enzymes. In glioblastoma cells, KGDHC is also detected in the nucleus, where the production of succinyl-CoA modifies histones and alters gene expression. Hence, DLST may also exert non–TCA cycle functions in neuroblastoma cells.

Emerging evidence demonstrates that many tumors rely on OXPHOS for their heightened bioenergetic and biosynthetic processes (34–43). Both metastatic melanoma and breast cancer undergo a bioenergetic shift, where OXPHOS predominates as the primary metabolic pathway for ATP production (44, 45). *MYCN* amplification can enhance OCR through upregulation of ETC components in neuroblastoma cells (14). Importantly, we found that high *DLST* expression significantly correlates with an enriched OXPHOS gene signature among patients with high-risk neuroblastoma. Treatment with multiple OXPHOS inhibitors impairs growth and induces apoptosis in neuroblastoma cells. OXPHOS can promote a migratory and invasive phenotype within breast cancer (46), and represents a mechanism underlying drug resistance in several other types of cancer (36, 47–50). It is likely that DLST enhances OXPHOS to support the growth, survival, and migration of neuroblastoma cells, thereby promoting disease aggression (Supplementary Fig. S7D).

Despite intensive multimodal therapy, the long-term survival of patients with high-risk neuroblastoma is very poor, especially for those with disease recurrence (4). Although the genetics of human neuroblastoma has been extensively studied, actionable therapeutics are limited (51). Recently, IACS-010759 was shown to exhibit preclinical efficacy in the treatment of AML, *SWI/SNF*–mutant lung cancer, mantle cell lymphoma, and melanoma (24, 45, 52–54). Our studies revealed that human neuroblastoma cells are acutely sensitive to IACS treatment, which slowed tumor growth in zebrafish and mouse xenografts. Therefore, OXPHOS represents an actionable target for high-risk neuroblastoma. Phase I clinical trials are currently being completed in adults with AML and solid tumors to determine the safety and antitumor efficacy of IACS (NCT #02882321 and #03291938). Further preclinical testing of IACS will determine whether this compound has clinical benefits in neuroblastoma. Like many other targeted therapies, IACS will likely need to be combined with either standard-of-care chemotherapy or other agents to lower dosing and decrease toxicity in pediatric patients. It will be critical to strategize on how IACS could be

successfully integrated into the standard treatment regimen for all patients with high-risk neuroblastoma, including those with *MYCN* amplification.

Supplementary Material

Refer to Web version on PubMed Central for supplementary material.

Acknowledgments

The authors thank members of the Simon and Feng labs for helpful discussions. They also thank John Tobias for help with processing the RNA-seq data, and O. Horyn and Ilanna Nissim for performing the isotopomer enrichment analysis and metabolite measurements in the Metabolomics Core Facility, Children's Hospital of Philadelphia. Christopher Petucci and the Penn Metabolomics core also provided technical assistance with metabolite measurements. N.M. Anderson was supported by a Young Investigator Grant from the Alex's Lemonade Stand Foundation (GR-000000165). J. Athoe and A. Lam acknowledge the Undergraduate Research Opportunity Award from Boston University. J. Athoe and A. Kennedy acknowledge Pediatric Oncology Student Training Awards from the Alex's Lemonade Stand Foundation. A.T. Look acknowledges grant support from National Institutes of Health (NIH) R35CA210064 and other granting sources. M.C. Simon acknowledges grant support from the NIH (P01 CA104838 and R35 CA197602). H. Feng acknowledges grant support from the NIH (CA134743 and CA215059), Boston University (1UL1TR001430 and Ralph Edwards Career Development Professorship), the Leukemia Research Foundation (Young Investigator Award), the American Cancer Society (RSG-17-204-01-TBG), and the St. Baldrick Foundation (Career Development Scholar Award).

Authors' Disclosures

N.M. Anderson reports grants from Alex's Lemonade Stand Foundation during the conduct of the study. X. Qin reports grants from Boston University, Ignition Award, Cure Research, ACS, and R01 during the conduct of the study. A. Lam reports grants from Boston University, Ignition Award, Cure Research, American Cancer Society, and R01 during the conduct of the study. J. Athoe reports grants from Alex's Lemonade Stand POST Grant during the conduct of the study. A. Kennedy reports grants from Alex's Lemonade Stand Foundation during the conduct of the study. A. Look reports grants from NIH R35CA210064 (A.T. Look) during the conduct of the study. A.T. Look is a shareholder in Jengu Therapeutics and is a consultant/advisory board member for Jengu Therapeutics and Omega Therapeutics. H. Feng reports grants from National Institution of Health, St. Baldrick's Foundation, Boston University, American Cancer Society, and Leukemia Research Foundation during the conduct of the study. No disclosures were reported by the other authors.

References

1. Brodeur GM. Neuroblastoma: biological insights into a clinical enigma. Nat Rev Cancer 2003;3:203–16. [PubMed: 12612655]
2. Maris JM. Recent advances in neuroblastoma. N Engl J Med 2010;362:2202–21. [PubMed: 20558371]
3. Pinto NR, Applebaum MA, Volchenboum SL, Matthay KK, London WB, Ambros PF, et al. Advances in risk classification and treatment strategies for neuroblastoma. J Clin Oncol 2015;33:3008–17. [PubMed: 26304901]
4. Park JR, Bagatell R, London WB, Maris JM, Cohn SL, Mattay KM, et al. Children's Oncology Group's 2013 blueprint for research: Neuroblastoma. Pediatr Blood Cancer 2013;60:985–93. [PubMed: 23255319]
5. Maris JM, Hogarty MD, Bagatell R, Cohn SL. Neuroblastoma seminar. Lancet 2007;369:2106–20. [PubMed: 17586306]
6. Zimmerman MW, Liu Y, He S, Durbin AD, Abraham BJ, Easton J, et al. MYC drives a subset of high-risk pediatric neuroblastomas and is activated through mechanisms including enhancer hijacking and focal enhancer amplification. Cancer Discov 2018;8:320–35. [PubMed: 29284669]
7. Zhu S, Lee JS, Guo F, Shin J, Perez-Atayde AR, Kutok JL, et al. Activated ALK collaborates with MYCN in neuroblastoma pathogenesis. Cancer Cell 2012;21: 362–73. [PubMed: 22439933]
8. Berry T, Luther W, Bhatnagar N, Jamin Y, Poon E, Sanda T, et al. The ALKF1174L mutation potentiates the oncogenic activity of MYCN in neuroblastoma. Cancer Cell 2012;22:117–30. [PubMed: 22789543]

9. Heukamp LC, Thor T, Schramm A, De Preter K, Kumps C, De Wilde B, et al. Targeted expression of mutated ALK induces neuroblastoma in transgenic mice. Sci Transl Med 2012;4:141ra91.
10. Tao T, Sondalle SB, Shi H, Zhu S, Perez-Atayde AR, Peng J, et al. The pre-rRNA processing factor DEF is rate limiting for the pathogenesis of MYCN-driven neuroblastoma. Oncogene 2017;36:3852–67. [PubMed: 28263972]
11. Zhu S, Zhang X, Weichert-Leahey N, Dong Z, Zhang C, Lopez G, et al. LMO1 synergizes with MYCN to promote neuroblastoma initiation and metastasis. Cancer Cell 2017;32:310–23. [PubMed: 28867147]
12. Wang K, Diskin SJ, Zhang H, Attiyeh EF, Winter C, Hou C, et al. Integrative genomics identifies LMO1 as a neuroblastoma oncogene. Nature 2011;469: 216–20. [PubMed: 21124317]
13. Stine ZE, Walton ZE, Altman BJ, Hsieh AL, Dang CV. MYC, metabolism, and cancer. Cancer Discov 2015;5:1024–39. [PubMed: 26382145]
14. Oliynyk G, Ruiz-Pérez MV, Sainero-Alcolado L, Dzieran J, Zirath H, Gallart-Ayala H, et al. MYCN-enhanced oxidative and glycolytic metabolism reveals vulnerabilities for targeting neuroblastoma. iScience 2019;21:188–204. [PubMed: 31670074]
15. Qing G, Li B, Vu A, Skuli N, Walton ZE, Liu X, et al. ATF4 regulates MYC-mediated neuroblastoma cell death upon glutamine deprivation. Cancer Cell 2012;22:631–44. [PubMed: 23153536]
16. Xia Y, Ye B, Ding J, Yu Y, Alptekin A, Thangaraju M, et al. Metabolic reprogramming by MYCN confers dependence on the serine-glycine-one-carbon biosynthetic pathway. Cancer Res 2019;79:3837–50. [PubMed: 31088832]
17. Chandel NS. Navigating metabolism. Cold Spring Harbour: Cold Spring Harbor Laboratory Press; 2015.
18. Ilic N, Birsoy K, Aguirre AJ, Kory N, Pacold ME, Singh S, et al. PIK3CA mutant tumors depend on oxoglutarate dehydrogenase. Proc Natl Acad Sci U S A 2017; 114:E3434–43. [PubMed: 28396387]
19. Allen EL, Ulanet DB, Pirman D, Mahoney CE, Coco J, Si Y, et al. Differential aspartate usage identifies a subset of cancer cells particularly dependent on OGDH. Cell Rep 2016;17:876–90. [PubMed: 27732861]
20. Wang Y, Guo YR, Liu K, Yin Z, Liu R, Xia Y, et al. KAT2A coupled with the α-KGDH complex acts as a histone H3 succinyltransferase. Nature 2017;552: 273–7. [PubMed: 29211711]
21. Remacha L, Pirman D, Mahoney CE, Coloma J, Calsina B, Currás-Freixes M, et al. Erratum: Recurrent germline DLST mutations in individuals with multiple pheochromocytomas and paragangliomas. Am J Hum Genet 2019;104:651–64. [PubMed: 30929736]
22. Anderson NM, Li D, Peng HL, Laroche FJF, Mansour MR, Gjini E, et al. The TCA cycle transferase DLST is important for MYC-mediated leukemogenesis. Leukemia 2016;30:1365–74. [PubMed: 26876595]
23. Westerfield M The Zebrafish Book: A Guide for the Laboratory Use of Zebrafish (Brachydanio rerio). Eugene: University of Oregon Press; 1994.
24. Molina JR, Sun Y, Protopopova M, Gera S, Bandi M, Bristow C, et al. An inhibitor of oxidative phosphorylation exploits cancer vulnerability. Nat Med 2018;24:1036–46. [PubMed: 29892070]
25. Su Z, Fang H, Hong H, Shi L, Zhang W, Zhang W, et al. An investigation of biomarkers derived from legacy microarray data for their utility in the RNA-seq era. Genome Biol 2014;15:523. [PubMed: 25633159]
26. Molenaar JJ, Koster J, Zwijnenburg DA, Van Sluis P, Valentijn LJ,Van Der Ploeg I, et al. Sequencing of neuroblastoma identifies chromothripsis and defects in neuritogenesis genes. Nature 2012;483:589–93. [PubMed: 22367537]
27. Tao T, Sondalle SB, Shi H, Zhu S, Perez-Atayde AR, Peng J, et al. The pre-rRNA processing factor DEF is rate limiting for the pathogenesis of MYCN-driven neuroblastoma. Oncogene 2017;36:3852–67. [PubMed: 28263972]
28. Amsterdam A, Nissen RM, Sun Z, Swindell EC, Farrington S, Hopkins N. Identification of 315 genes essential for early zebrafish development. Proc Natl Acad Sci U S A 2004;101:12792–7. [PubMed: 15256591]

29. Heart E, Yaney GC, Corkey RF, Schultz V, Luc E, Liu L, et al. Ca2+, NAD(P)H and membrane potential changes in pancreatic β-cells by methyl succinate: Comparison with glucose. Biochem J 2007;403:197–205. [PubMed: 17181533]
30. Sica V, Bravo-San Pedro JM, Izzo V, Pol J, Pierredon S, Enot D, et al. Lethal poisoning of cancer cells by respiratory chain inhibition plus dimethyl α-keto-glutarate. Cell Rep 2019;27:820–34. [PubMed: 30995479]
31. Xiao D, Ren P, Su H, Yue M, Xiu R, Hu Y, et al. Myc promotes glutaminolysis in human neuroblastoma through direct activation of glutaminase 2. Oncotarget 2015;6:40655–66. [PubMed: 26528759]
32. Remacha L, Pirman D, Mahoney CE, Coloma J, Calsina B, Currás-Freixes M, et al. Recurrent germline DLST mutations in individuals with multiple pheochromocytomas and paragangliomas. Am J Hum Genet 2019;104:651–64. [PubMed: 30929736]
33. Shim EH, Livi CB, Rakheja D, Tan J, Benson D, Parekh V, et al. L-2-hydroxyglutarate: an epigenetic modifier and putative oncometabolite in renal cancer. Cancer Discov 2014;4:1290–8. [PubMed: 25182153]
34. Caro P, Kishan AU, Norberg E, Stanley IA, Chapuy B, Ficarro SB, et al. Metabolic signatures uncover distinct targets in molecular subsets of diffuse large B cell lymphoma. Cancer Cell 2012;22:547–60. [PubMed: 23079663]
35. Goto M, Miwa H, Shikami M, Tsunekawa-Imai N, Suganuma K, Mizuno S, et al. Importance of glutamine metabolism in leukemia cells by energy production through TCA cycle and by redox homeostasis. Cancer Invest 2014;32:241–7. [PubMed: 24762082]
36. Vazquez F, Lim JH, Chim H, Bhalla K, Girnun G, Pierce K, et al. PGC1α expression defines a subset of human melanoma tumors with increased mitochondrial capacity and resistance to oxidative stress. Cancer Cell 2013; 23:287–301. [PubMed: 23416000]
37. Viale A, Pettazzoni P, Lyssiotis CA, Ying H, Sánchez N, Marchesini M, et al. Oncogene ablation-resistant pancreatic cancer cells depend on mitochondrial function. Nature 2014;514:628–32. [PubMed: 25119024]
38. Birsoy K, Wang T, Chen WW, Freinkman E, Abu-Remaileh M, Sabatini DM. An essential role of the mitochondrial electron transport chain in cell proliferation is to enable aspartate synthesis. Cell 2015;162:540–51. [PubMed: 26232224]
39. Sullivan LB, Gui DY, Hosios AM, Bush LN, Freinkman E, Vander Heiden MG. Supporting aspartate biosynthesis is an essential function of respiration in proliferating cells. Cell 2015;162:552–63. [PubMed: 26232225]
40. Haq R, Shoag J, Andreu-Perez P, Yokoyama S, Edelman H, Rowe GC, et al. Oncogenic BRAF regulates oxidative metabolism via PGC1α and MITF. Cancer Cell 2013;23:302–15. [PubMed: 23477830]
41. Roesch A, Vultur A, Bogeski I, Wang H, Zimmermann KM, Speicher D, et al. Overcoming intrinsic multidrug resistance in melanoma by blocking the mitochondrial respiratory chain of slow-cycling JARID1B(high) cells. Cancer Cell 2013;23:811–25. [PubMed: 23764003]
42. Simsek T, Kocabas F, Zheng J, Deberardinis RJ, Mahmoud AI, Olson EN, et al. The distinct metabolic profile of hematopoietic stem cells reflects their location in a hypoxic niche. Cell Stem Cell 2010;7:380–90. [PubMed: 20804973]
43. Hu J, Locasale JW, Bielas JH, O'Sullivan J, Sheahan K, Cantley LC, et al. Heterogeneity of tumor-induced gene expression changes in the human metabolic network. Nat Biotechnol 2013;31:522–9. [PubMed: 23604282]
44. Davis RT, Blake K, Ma D, Gabra MBI, Hernandez GA, Phung AT, et al. Transcriptional diversity and bioenergetic shift in human breast cancer metastasis revealed by single-cell RNA sequencing. Nat Cell Biol 2020;22:310–20. [PubMed: 32144411]
45. Fischer GM, Jalali A, Kircher DA, Lee WC, McQuade JL, Haydu LE, et al. Molecular profiling reveals unique immune and metabolic features of melanoma brain metastases. Cancer Discov 2019;9:628–45. [PubMed: 30787016]
46. LeBleu VS, O'Connell JT, Gonzalez Herrera KN, Wikman H, Pantel K, Haigis MC, et al. PGC-1a mediates mitochondrial biogenesis and oxidative phosphorylation to promote metastasis. Nat Cell Biol 2014;16:992–1003. [PubMed: 25241037]

47. Lee KM, Giltnane JM, Balko JM, Schwarz LJ, Guerrero-Zotano AL, Hutchinson KE, et al. MYC and MCL1 cooperatively promote chemotherapy-resistant breast cancer stem cells via regulation of mitochondrial oxidative phosphorylation. Cell Metab 2017;26:633–47. [PubMed: 28978427]

48. Farge T, Saland E, de Toni F, Aroua N, Hosseini M, Perry R, et al. Chemotherapy-resistant human acute myeloid leukemia cells are not enriched for leukemic stem cells but require oxidative metabolism. Cancer Discov 2017;7:716–35. [PubMed: 28416471]

49. Hirpara J, Eu JQ, Tan JKM, Wong AL, Clement MV, Kong LR, et al. Metabolic reprogramming of oncogene-addicted cancer cells to OXPHOS as a mechanism of drug resistance. Redox Biol 2019;25:101076. [PubMed: 30642723]

50. Kuntz EM, Baquero P, Michie AM, Dunn K, Tardito S, Holyoake TL, et al. Targeting mitochondrial oxidative phosphorylation eradicates therapy-resistant chronic myeloid leukemia stem cells. Nat Med 2017;23:1234–40. [PubMed: 28920959]

51. Matthay KK, Maris JM, Schleiermacher G, Nakagawara A, Mackall CL, Diller L, et al. Neuroblastoma. Nat Rev Dis Prim 2016;2:16078. [PubMed: 27830764]

52. Lissanu Deribe Y, Sun Y, Terranova C, Khan F, Martinez-Ledesma J, Gay J, et al. Mutations in the SWI/SNF complex induce a targetable dependence on oxidative phosphorylation in lung cancer article. Nat Med 2018;24:1047–57. [PubMed: 29892061]

53. Gopal YNV, Gammon S, Prasad R, Knighton B, Pisaneschi F, Roszik J, et al. A novel mitochondrial inhibitor blocks MAPK pathway and overcomes MAPK inhibitor resistance in melanoma. Clin Cancer Res 2019;25:6429–42. [PubMed: 31439581]

54. Zhang L, Yao Y, Zhang S, Liu Y, Guo H, Ahmed M, et al. Metabolic reprogramming toward oxidative phosphorylation identifies a therapeutic target for mantle cell lymphoma. Sci Transl Med 2019;11:eaau1167. [PubMed: 31068440]

Significance:

These findings demonstrate a novel role for DLST in neuroblastoma aggression and identify the OXPHOS inhibitor IACS-010759 as a potential therapeutic strategy for this deadly disease.

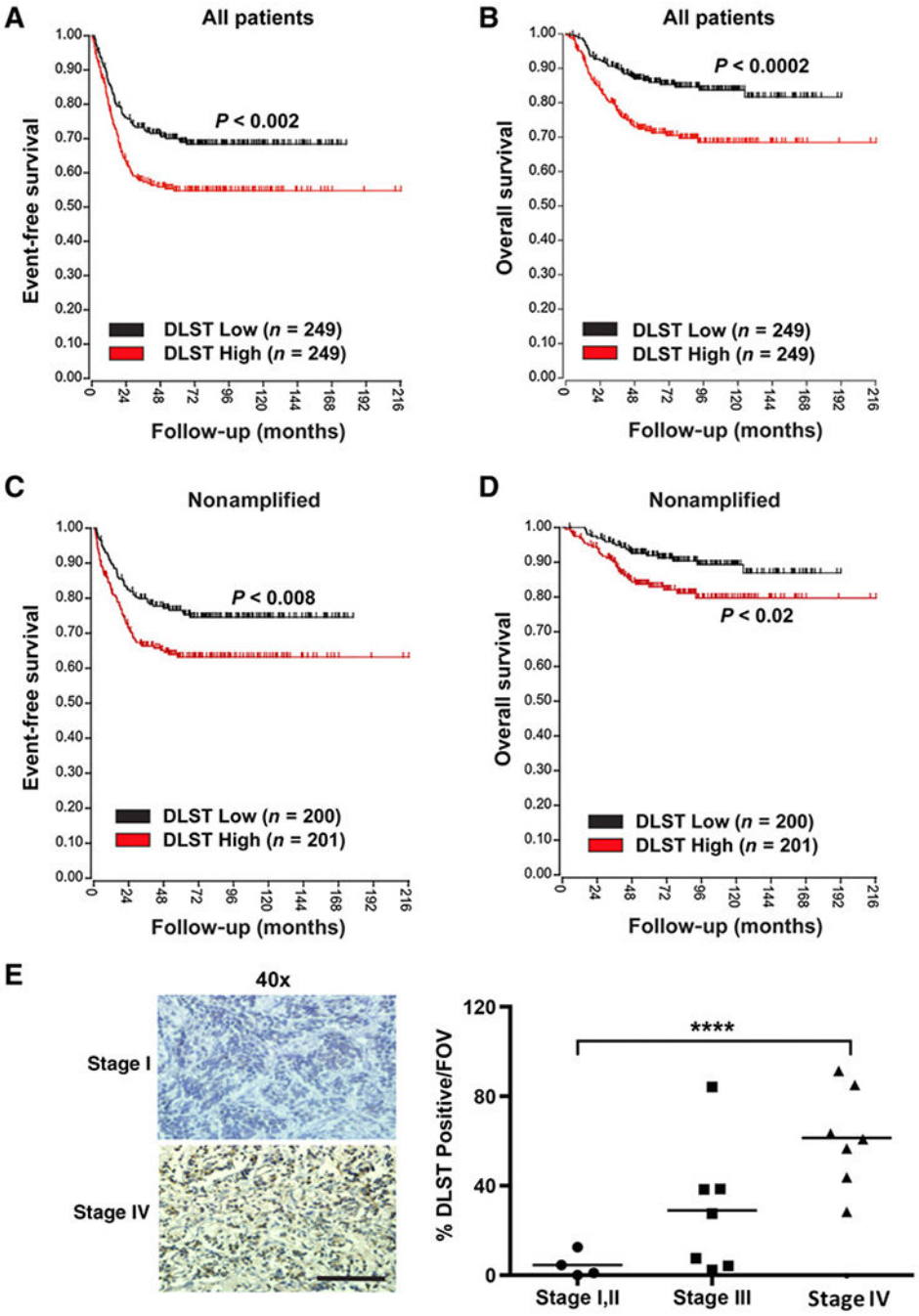

Figure 1.

High *DLST* expression predicts poor outcomes and tumor aggression in patients with neuroblastoma. **A–D,** Kaplan–Meier survival curves illustrate a negative association between high *DLST* expression and poor event-free and overall survival: total cohort (**A** and **B,** median; low vs. high *DLST* expression, $n = 249$) and a nonamplified subcohort (**C** and **D,** median; $n = 200$ or 201) of patients with neuroblastoma. All data were analyzed for a public database in the R2: genomics analysis and visualization platform (GEO: GSE62564). **A–D,** Statistical significance was determined by survival analysis and calculated with the

log-rank test. **E,** Immunohistochemical analyses of primary neuroblastoma patient samples show significantly increased DLST protein levels in advanced stage IV tumors ($n = 4–7$). Scale bar, 50 μm. Statistical significance: ***, $P < 0.0001$; calculated with an unpaired *t* test unless otherwise stated.

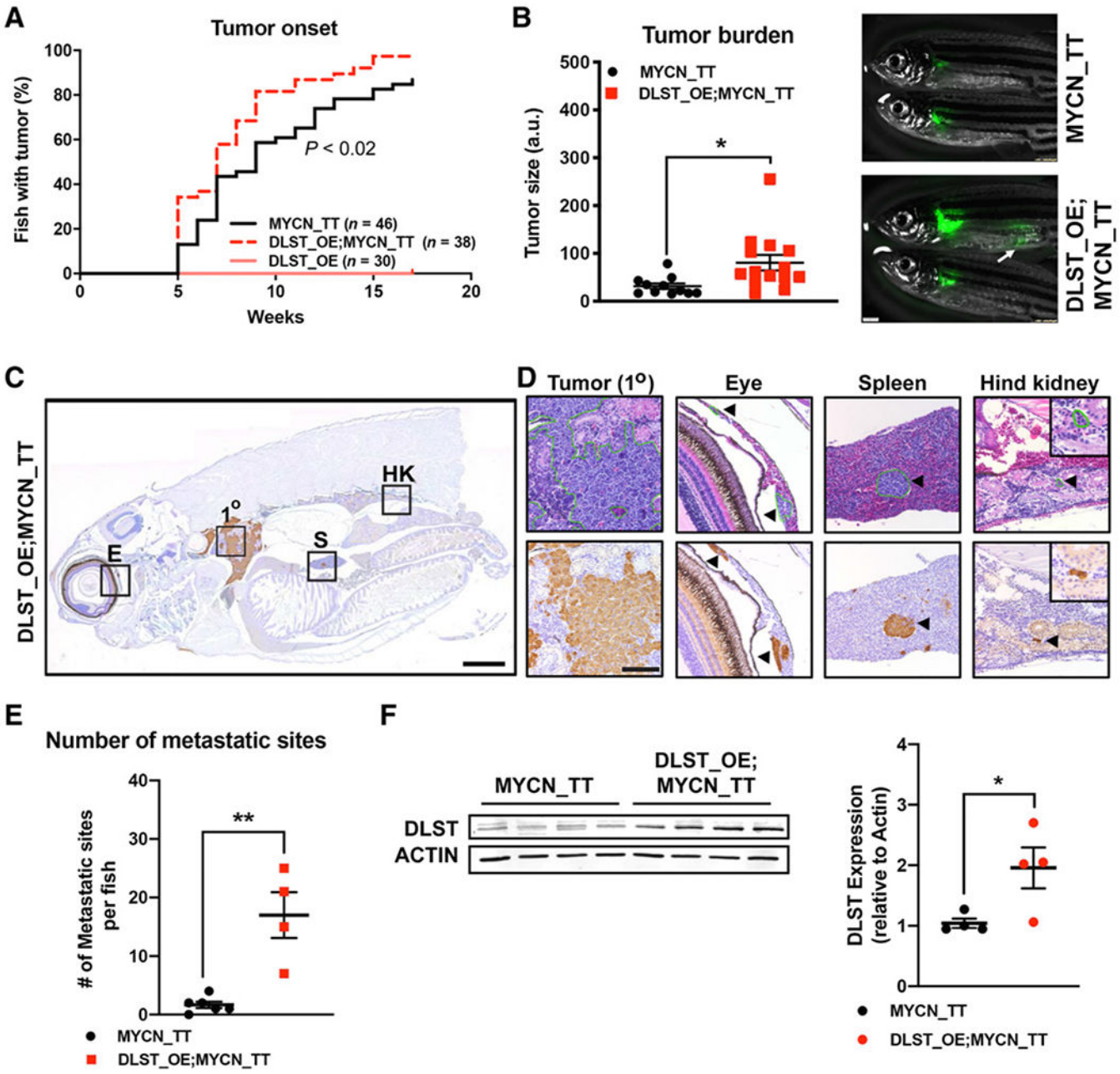

Figure 2.

DLST overexpression promotes MYCN-driven tumor aggression in zebrafish. **A,** Rates of tumor induction show that *DLST* overexpression accelerates neuroblastoma onset (MYCN_*TT* vs. DLST_OE;MYCN_TT, $n = 38$-46; $P = 0.015$). Overexpression of *DLST* alone (DLST_OE) was insufficient to induce neuroblastoma development. Statistical analysis was performed by the log-rank Mantel-Cox test. **B,** Quantification of EGFP fluorescent intensity revealed increased tumor burden in 6-wpf DLST_OE;MYCN_TT transgenic fish, compared with MYCN_TT fish (left; $n = 11$-14). Overlay of brightfield and EGFP images of two MYCN_TT and DLST_OE;MYCN_TT fish (right). White

arrow indicates tumors distant from the interrenal gland (IRG) in DLST_OE;MYCN_TT fish. Scale bar, 1 mm. **C–E,** *DLST* overexpression in the MYCN_TT fish increases the incidence of metastasis. **C,** Sagittal sections of DLST_OE;MYCN_TT fish at 6-wpf were immunostained with TH antibody and hematoxylin counterstain. E, sclera of the eyes, S, spleen; HK, hind kidney. **D,** Magnified views of TH-stained sections (bottom panels) or hematoxylin and eosin–stained adjacent sections (top panels). The black box with the 1° label indicates the IRG (site of the primary tumor). Scale bar, 1mm(**C**); 100 μm (**D**). Black arrows indicate tumor cells at distant sites: sclera of the eyes, spleen, and hind kidney. Insets in the right two panels are a close-up view of tumor cells in the hind kidney. **E,** The number of metastatic sites per fish (MYCN_TT vs. DLST_OE;MYCN_TT, $n = 4–6$). **F,** Western blotting analysis of tumor cells demonstrated approximately two-fold higher DLST levels in DLST_OE;MYCN_TT fish versus MYCN_TT fish ($n=4$). Data are presented as mean ± SEM, unless otherwise stated. Statistical significance: *, $P < 0.02$; **, $P=0.0014$.

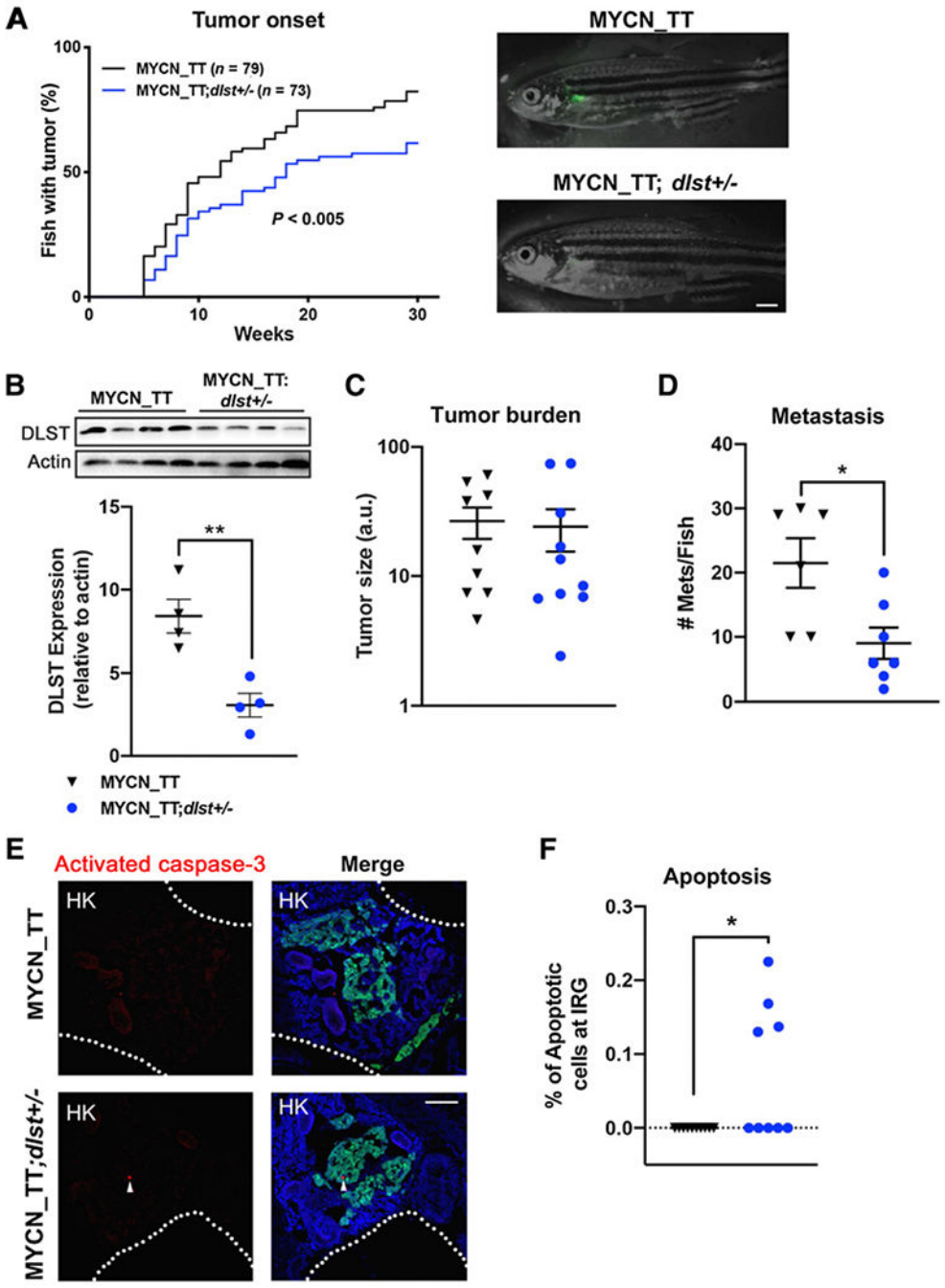

Figure 3.

Heterozygous loss of *dlst* delays neuroblastoma onset, reduces disease aggression, and induces apoptotic cell death at the IRG of *MYCN* fish. **A,** Rates of tumor induction indicate that heterozygous-loss of *dlst* delays MYCN-driven neuroblastoma onset (MYCN_TT vs. MYCN_TT;dlst±: $P < 0.005$). Statistical analysis was performed by the log-rank Mantel–Cox test. Neuroblastoma developed in a 6-wpf MYCN_TT fish (top), while no tumor developed in its sibling MYCN_TT; *dlst*± fish (bottom). Scale bar, 1 mm. **B,** Western blotting confirmed a 50% reduction of DLST protein levels in tumor cells from

MYCN_TT; *dlst*±fish, compared with those from their MYCN_TT siblings ($n = 4$). **C,** Quantification of EGFP fluorescent intensity revealed no alteration in tumor burden in 10-wpf MYCN_TT;dlst± transgenic fish, compared with MYCN_TT fish ($n = 11–14$). **D,** The number of metastatic sites per fish (MYCN_TT vs. MYCN_TT; *dlst*±; $n = 6–7$). **E** and **F,** Heterozygous loss of *dlst* results in apoptosis at the IRG of the 3-wpf fish. Green, sagittal sections of MYCN_TT and MYCN_TT; *dlst*±fish at 3-wpf: tumor cells; red, activated caspase-3 ($AC3^+$); blue, DAPI (left). White arrowheads indicate $AC3^+$ cells and dotted lines the boundary of the hind kidney (HK). Percentage of $AC3^+$ among the total number of $EGFP^+$ sympathetic neuroblasts at the IRG of 3-wpf MYCN_TT and MYCN_TT; *dlst*±fish (right; n=9–10). Scale bar, 50 μmol/L. Statistical significance: *, $P \leq 0.05$; **, $P \leq 0.01$.

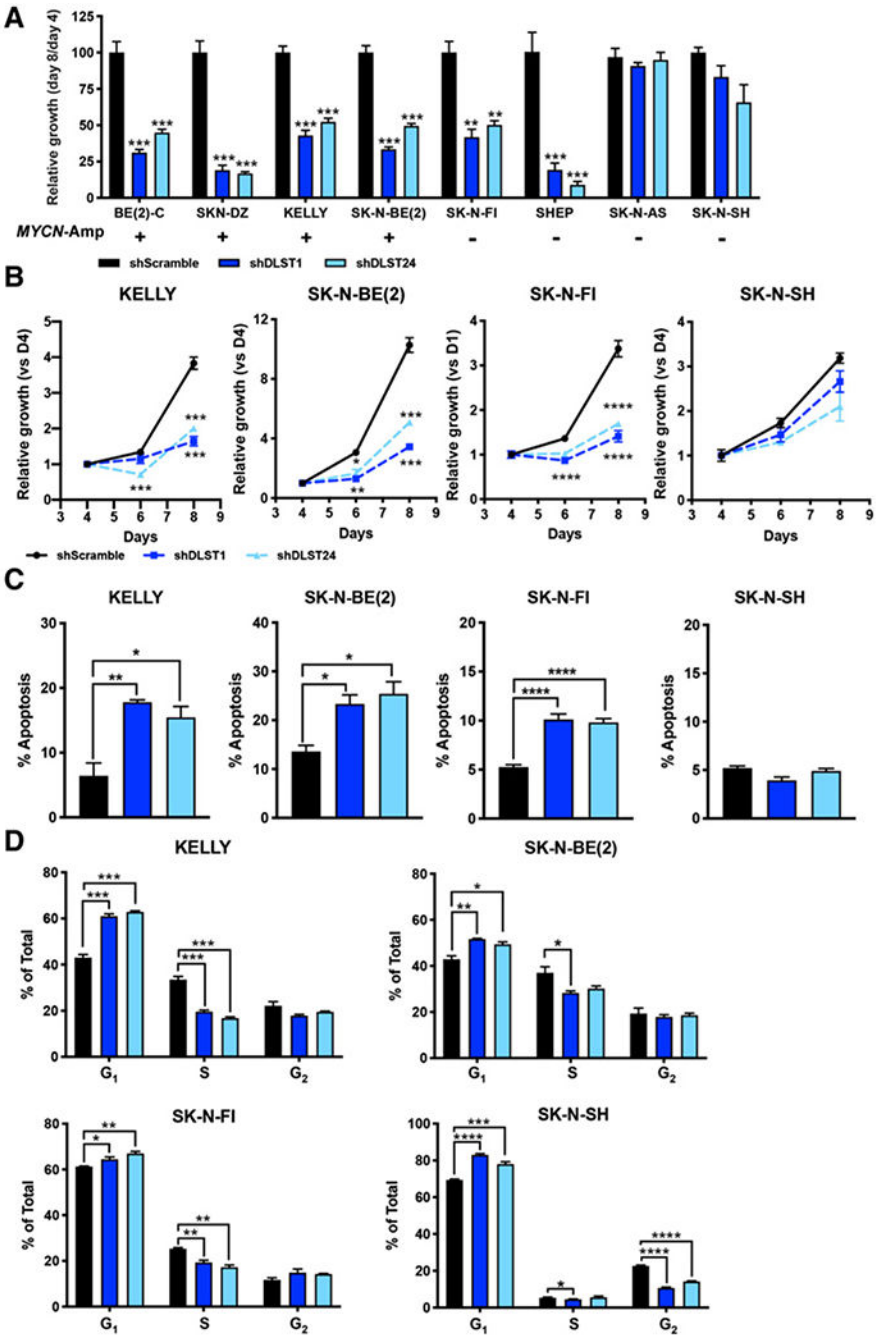

Figure 4.

DLST depletion by RNAi slows growth, alters cell cycle, and increases apoptosis of human *MYCN*-amplified neuroblastoma cells. **A,** Relative growth rates of a panel of human neuroblastoma cell lines upon DLST depletion: *MYCN*-amplified BE(2)-C, SK-N-DZ, KELLY, and SK-N-BE(2), and nonamplified SK-N-FI, SHEP, SK-N-SH, and SK-N-AS (n = 4). **B,** The growth kinetics of human neuroblastoma cells were analyzed after transducing with either *shScramble* or two *shRNA* hairpins targeting *DLST*: *MYCN*-amplified cell lines KELLY and SK-N-BE(2), and nonamplified cell lines SK-N-FI and SK-N-SH (n = 4). **C,**

Apoptosis was induced by *shDLST* in *MYCN*-amplified cell lines: KELLY, SK-N-BE(2), and SK-N-FI, but not in nonamplified SK-N-SH. Annexin V and PI staining was performed on cells isolated at 5 days postinfection ($n = 4$). **D,** *DLST* inactivation induces cell-cycle alterations in KELLY, SK-N-BE(2), SK-N-FI, and SK-N-SH cell lines ($n = 4$). At 5 days postinfection, neuroblastoma cells were fixed and then stained with PI for flow cytometry analysis. Statistical significance: *,$P \leq 0.05$; **, $P \leq 0.01$; ***, $P \leq 0.001$;, **** $P \leq 0.0001$.

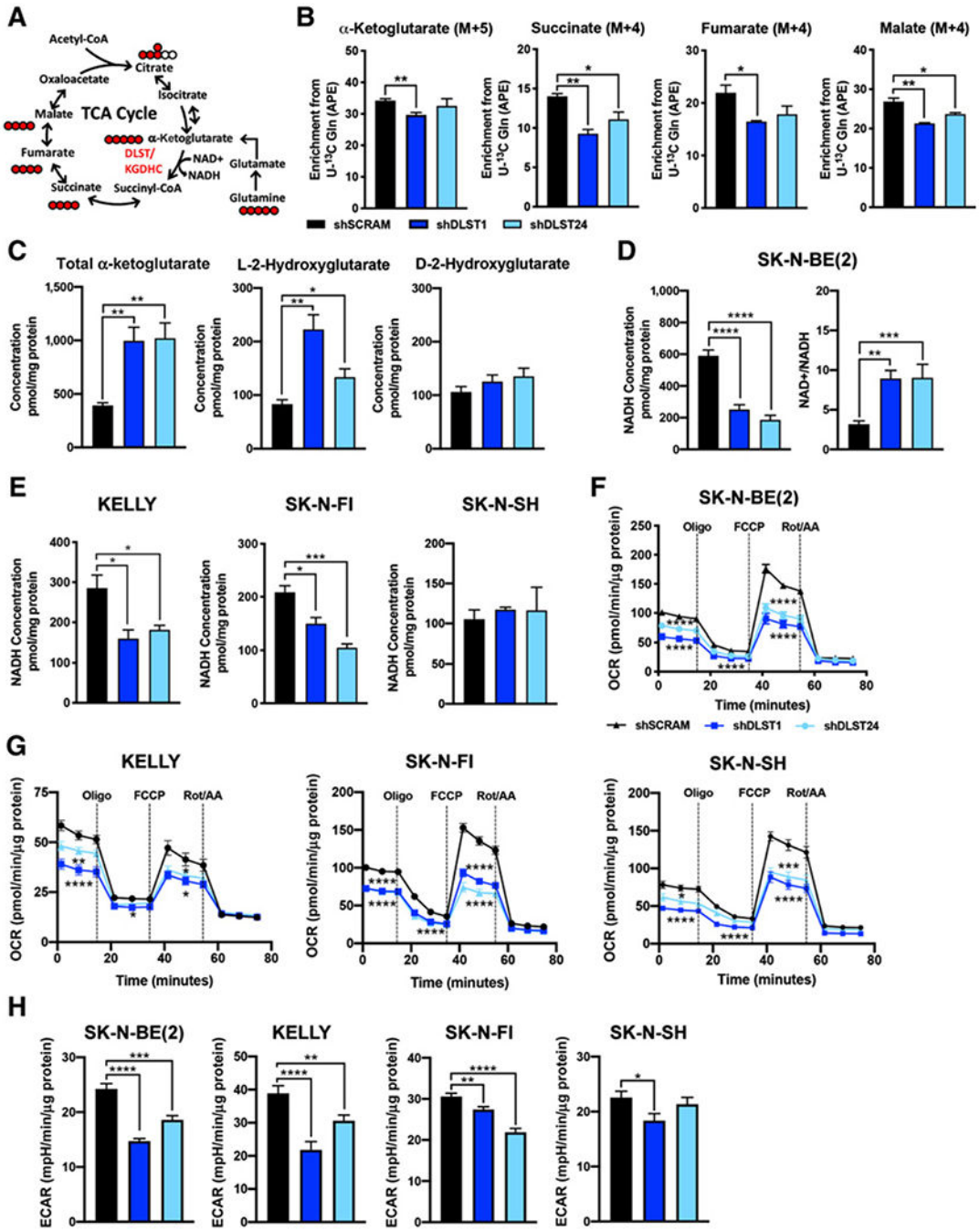

Figure 5.

DLST inactivation disrupts the TCA cycle and OXPHOS. **A,** Schematic of the TCA cycle indicating the location of DLST and a carbon fate map illustrating the distribution of metabolites derived from [µL-^{13}C]glutamine. Red-filled circles indicate 13-C atoms and empty circles indicate other carbon sources. **B,** Uniformly labeled [(µL)-$_{13}$C] glutamine M+4/5 distribution of TCA-cycle intermediates in SK-N-BE(2) after DLST depletion at 3.5-days post-infection ($n = 3$). **C,** Total intracellular αKG increases and L-2-HG accumulates in SK-N-BE(2) upon DLST depletion ($n = 3$). **D** and **E,** Intracellular NADH decreases

upon DLST depletion in SK-N-BE(2), KELLY, and SK-N-FI (n=4–5). **F** and **G,** Relative oxygen consumption rate (OCR) normalized to protein abundance in SK-N-BE(2), KELLY, SK-N-FI, and SK-N-SH after *DLST* inactivation (n = 12). **H,** Upon *DLST* depletion, the basal extracellular acidification rate (ECAR) dropped significantly in SK-N-BE(2), KELLY, and SK-N-FI (n=8–12). All experiments were performed 3.5 days before any evidence of cellular toxicity. Statistical significance: *, $P \leq 0.05$; **, $P \leq 0.01$; ***, $P \leq 0.001$;, **** $P \leq 0.0001$.

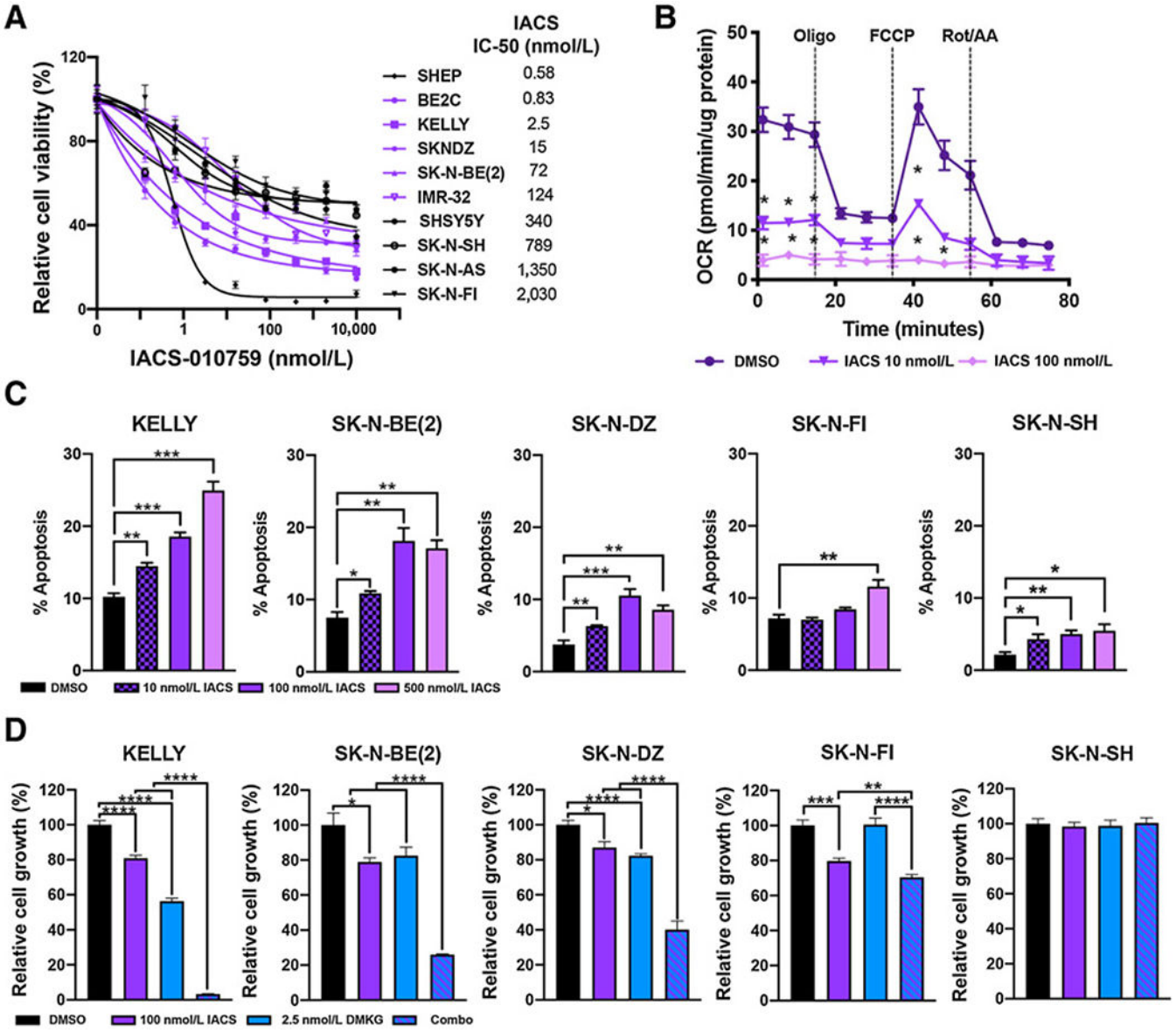

Figure 6.

Human neuroblastoma cells are sensitive to inhibitors of the ETC complex I. **A,** Dose–response curves and their IC_{50}s for a panel of human neuroblastoma cell lines treated with IACS for 5 days (n=6). IC_{50}s were calculated with log(inhibitor) versus normal response. **B,** The relative OCR for the cell line KELLY after 24 hours of IACS treatment (n = 12). **C,** IACS induced a dose-dependent induction of apoptosis in KELLY, SK-N-BE(2), SK-N-DZ, SK-N-FI, and SK-N-SH after 5 days of treatment by Annexin V and PI staining (n=4–5). **D,** DMKG and IACS show striking synergy upon 48-hour treatment in KELLY, SK-N-BE(2), SK-N-DZ, and SK-N-FI, but not in SK-N-SH cells (n = 6). Statistical significance: *, $P \leq 0.05$; **, $P \leq 0.01$; ***, $P \leq 0.001$; ****, $P \leq 0.0001$.

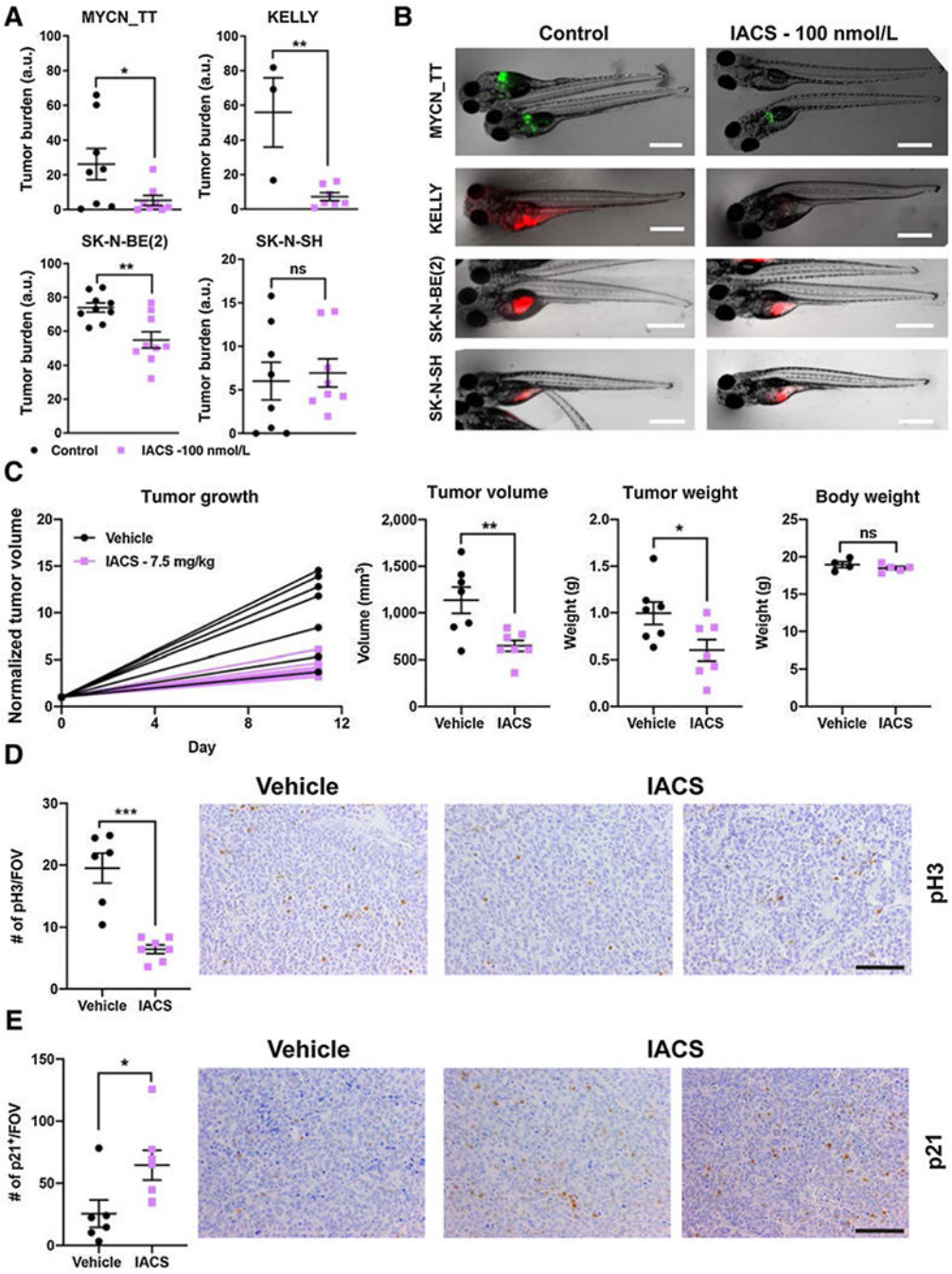

Figure 7.

OXPHOS inhibition by IACS slows the growth of *MYCN*-amplified neuroblastoma xenografts. **A** and **B,** Zebrafish xenografts (MYCN_TT or human *MYCN*-amplified neuroblastoma cells) demonstrate sensitivity to 100 nmol/L of IACS (96 hours, MYCN_TT; 72 hours, KELLY, SK-N-BE(2), and SK-N-SH; $n = 3–8$; scale bar, 0.5 mm). **C,** Normalized tumor growth of subcutaneous KELLY xenografts in Balb/c nude mice treated with either vehicle or IACS by oral gavage ($n = 6–7$). Treatment was initiated once tumors reached approximately 100 mm^3. Final tumor volume and weight of KELLY xenografts after 11

days of IACS treatment ($n = 6–7$). Final body weight of mice after 11 days of treatment: vehicle versus IACS ($n=4–5$). **D** and **E,** IACS treatment leads to a decrease in proliferative cells as indicated by pH3 staining and a cell-cycle arrest as determined by an increase of p21 staining per field of view (FOV; $n = 7$). Scale bars, 100 μm. Statistical significance: *, $P \leq 0.05$; **, $P \leq 0.01$;***, $P \leq 0.001$; ns, nonsignificant.